

Barely visible impact damage assessment in laminated composites using acoustic emission

Milad Saeedifar¹, Mehdi Ahmadi Najafabadi*¹, Dimitrios Zarouchas², Hossein Hosseini Toudeshky³, Meisam Jalalvand^{4,5}

1. Non-destructive Testing Lab, Department of Mechanical Engineering, Amirkabir University of Technology, 424 Hafez Ave, 15914, Tehran, Iran.
2. Structural Integrity & Composites Group, Faculty of Aerospace Engineering, Delft University of Technology, The Netherlands.
3. Department of Aerospace Engineering, Amirkabir University of Technology, 424 Hafez Ave, 15914, Tehran, Iran.
4. Department of Mechanical and Aerospace Engineering, The University of Strathclyde, 75 Montrose Street, Glasgow G1 1XJ, UK
5. Bristol Composites Institute, University of Bristol, Bristol BS8 1TR, UK

Abstract

Despite the key advantages of Fiber Reinforced Polymer (FRP) composites, they are susceptible to Barely Visible Impact Damage (BVID) under transverse loadings. This study investigates BVID in two quasi-isotropic carbon/epoxy laminates under quasi-static indentation and Low-Velocity Impact (LVI) loadings using Acoustic Emission (AE). First, the evolution of interlaminar and intralaminar damages is studied by analyzing the AE signals of the indentation test using b-value and sentry function methods. Then, the specimens are subjected to the LVI loading and the induced damages are compared with the indentation test and the percentage of each damage mechanism is calculated using Wavelet Packet Transform (WPT). In consistent with the mechanical data, ultrasonic C-scan and digital camera images of the specimens, the AE results show a considerable similarity between the induced BVID under quasi-static indentation and LVI tests. Finally, the obtained results show that AE is a powerful tool to study BVID in laminated composites under quasi-static and dynamic transverse loadings.

Keywords: Barely Visible Impact Damage; Indentation; Low-Velocity Impact; Acoustic Emission; Laminated Composites; b-value; sentry function; Wavelet Packet Transform.

* Corresponding author. Tel.: +98 21 6454 3431; fax: +98 21 8871 2838. E-mail address: ahmadin@aut.ac.ir (M. Ahmadi Najafabadi)

1. Introduction

Fiber Reinforced Polymer (FRP) composites have key advantages such as high specific strength and stiffness, high corrosion resistance, and high fatigue life [1-2]. Despite these advantages, they are susceptible to Barely Visible Impact Damage (BVID) under transverse loadings [3, 4]. Low-Velocity Impact (LVI) is a common transverse load that may be applied to a composite structure during its service life, such as dropping a tool on the laminate surface during maintenance process, bird strike phenomenon during airplane landing or takeoff, and impact of hailstones to the composite structures during a hailstorm [5]. The LVI-induced damages in a FRP laminate are generally divided into two groups; interlaminar damages such as delamination and intralaminar damages such as matrix cracking and fiber breakage. These damages usually occur inside the material without any significant evidence on the structure surface which are usually named BVID [6]. The damage detection process also gets more difficult for dark FRP composites such as carbon/epoxy in comparison to transparent FRP composites such as glass/epoxy. In this situation, Non-Destructive Evaluation (NDE) techniques are capable tools to detect BVID in the material.

Many researches have been conducted to detect BVID in laminated composites using different NDE techniques [7-11]. Polimeno et al. [12] used the Nonlinear Elastic Wave Spectroscopy (NEWS) to detect BVID in carbon fiber composite plates. The results showed that NEWS is able not only to detect the presence of delamination at the plies interfaces but also indicates the damage severity. Klepka et al. [13] detected the presence of delamination in impacted carbon/epoxy composites using the modal and nonlinear vibro-acoustic modulation tests. Sun et al. [6] used the X-ray Computed Tomography (CT) scanning and a 3D Finite Element (FE) model for the experimental and numerical detection of BVID in carbon/epoxy

laminates, respectively. The obtained results illustrated that the detected delaminations by CT scan are in accordance with the predicted delaminations by the FE model. Dziendzikowski et al. [14] detected and located impact-induced delamination in glass/epoxy laminates using an array of piezoelectric (PZT) transducers. They compared the performance of the embedded and attached PZT transducers to detect BVID and also proposed an algorithm based on a correlation analysis technique called RAPID (reconstruction algorithm for probabilistic inspection of defects) to localize the damages. Katunin et al. [15] identified BVID in three different composite structures consisting of a glass/epoxy composite plate, a GLARE plate, and finally, a CFRP composite structure reinforced with stiffeners that was extracted from a vertical stabilizer of an aircraft using PZT sensing, ultrasonic, thermography, and vibration-based inspection methods. The results showed that the application of PZT is limited to the rough condition monitoring and its results are dependent on the arrangement of the PZT transducers. Also, the sensitivity of the ultrasonic C-scan was higher than thermography, but the inspection process by thermography was faster than ultrasonic C-scan. Finally, although the vibration-based inspection presented acceptable results, its resolution was less than C-scan and thermography methods. Mustapha et al. [16] used the ultrasonic guided waves to detect BVID in CF/EP sandwich composites. They defined a damage index based on the change in the peak magnitude and time reversal method and then used this index to locate the damage position. All the mentioned researches have only focused on the detecting and localizing of impact-induced delamination by the active NDE techniques such as ultrasonic C-scan, CT scan, modal analysis, ultrasonic guided waves, thermography, etc. and they have not investigated other impact-induced intralaminar damages such as matrix cracking and fiber breakage and also the evolution behavior of these damages.

Acoustic Emission (AE) as a passive NDE technique has the capability for the online monitoring of the induced damages in laminated composites [17-22]. Pashmforoush et al. [23]

classified four different damage mechanisms in sandwich composites using AE and k-Means genetic algorithm. Mohammadi et al. [24], quantified damage mechanisms in Open Hole Tensile (OHT) glass/epoxy laminates using AE and wavelet analysis. The quantity of the clustered damages was in accordance with the results of the proposed continuum damage-based FE model.

Literature review shows that many studies have been conducted on the experimental, analytical, and numerical analysis of the impact-induced damages in laminated composites [25-30], but there is a lack in the case of AE-based study of BVID in these materials. Boominathan et al. [31] employed AE to characterize the effect of temperature on the impact-induced damages in carbon/epoxy composites. They did not directly monitor the impact process by AE and used the AE to monitor the quasi-static Compression After Impact (CAI) test on the impacted specimens. Saeedifar et al. [32] studied the performance of six different clustering methods containing k-Means, Genetic k-Means, Fuzzy C-Means, Self-Organizing Map (SOM), Gaussian Mixture Model (GMM), and hierarchical model to classify AE signals of the interlaminar and intralaminar damages in carbon/epoxy laminated composites under quasi-static indentation loading. The results showed the hierarchical model has the best performance to cluster the AE signals of the damage mechanisms. Suresh Kumar et al. [33] monitored the induced damages in hybrid laminated composites under repeated quasi-static indentation loading using AE. The rise angle of the AE signals and also the sentry function method were utilized to track the damage evolution in the specimens without study the evolution behavior of each damage mechanism, individually.

This paper focuses on the study of the evolution of barely visible interlaminar and intralaminar damages in carbon/epoxy laminated composites under quasi-static and LVI loading conditions using AE technique. First, specimens are subjected to the quasi-static indentation loading and the interlaminar and intralaminar damages are clustered based on their AE features.

Then, the evolution behavior of each damage mechanism is investigated using b-value and sentry function methods. In order to verify the AE results, ultrasonic C-scan and digital camera images are employed to detect BVID in the specimens. Afterward, the specimens are subjected to LVI loading and the mechanical behavior and their BVID are compared to the quasi-static indentation tests. In order to quantify the interlaminar and intralaminar damages in the impacted specimens, the recorded AE signals during the impact tests are analyzed by Wavelet Packet Transform (WPT) and energy content of each damage mechanism is specified. The C-scan and digital camera images of the LVI specimens are employed to verify the AE results of impact test. The AE-predicted percentages of each damage mechanism for LVI and quasi-static indentation loadings have a good consistency with each other. The obtained results show the applicability of AE to detect and distinguish BVID in laminated composites and also to track the evolution of different damage mechanisms under quasi-static and dynamic transverse loading conditions.

2. Experimental Procedures

2.1. Description of the Materials

The experimental tests were carried out on Hexcel IM7/8552 unidirectional carbon preregs cured according to the manufacturer's recommended procedure [34]. The physical and mechanical properties of IM7/8552 are represented in Table 1 [34, 35].

Table 1. The physical and mechanical properties of IM7/8552 [34, 35].

Physical properties	
Fiber density (g/cm ³)	1.77
Resin density (g/cm ³)	1.30
Fiber volume (%)	57.70
Laminate density (g/cm ³)	1.57

Mechanical properties	
E_1 (MPa)	161000
E_2 (MPa)	11400
E_3 (MPa)	11400
ν_{12}	0.300
ν_{23}	0.436
G_{12} (MPa)	5170
G_{13} (MPa)	5170
G_{23} (MPa)	3980

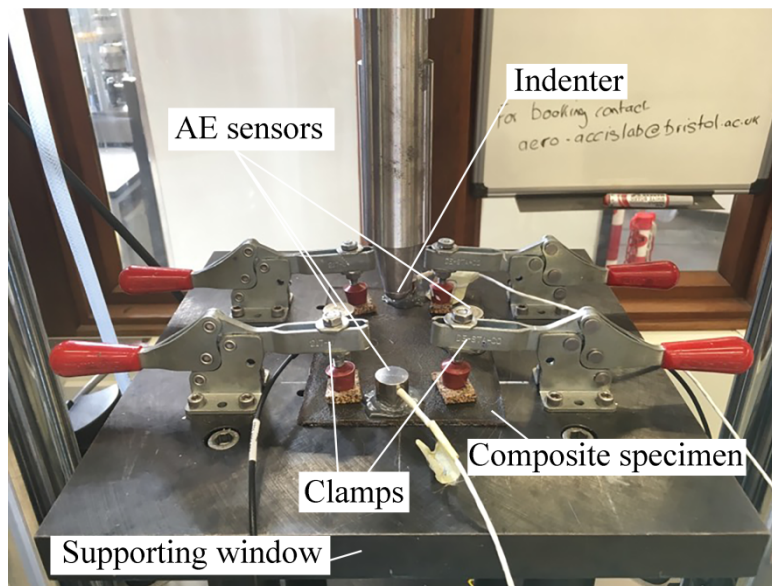
2.2. Test Method

In order to study the effect of **stacking sequence** on BVID, two quasi-isotropic laminates with the specified configurations in Table 2 were fabricated. The layup of the first specimen is $[60/0/-60]_{4S}$, which is named dispersed specimen and shown by S_D and the layup of the second specimen is $[60_4/0_4/-60_4]_S$ which is named blocked specimen and shown by S_B . The quasi-static indentation tests were conducted by pushing a $\Phi 16$ mm spherical-head indenter at the center of the rectangular specimen which was simply supported over a 125×75 mm² hollow window and was held by four clamps at its four corners. The tests were carried out under displacement control mode with the constant rate of 0.5 mm/min by an INSTRON servo-hydraulic testing machine **at the temperature of 25°C**. The machine continuously recorded the values of displacement and load during the tests. In order to capture the originated AE signals from the specimens under loading, four AE sensors were placed on the surface of the specimens (see Fig. 1.a). Three samples of each specimen type were tested to check the data repeatability.

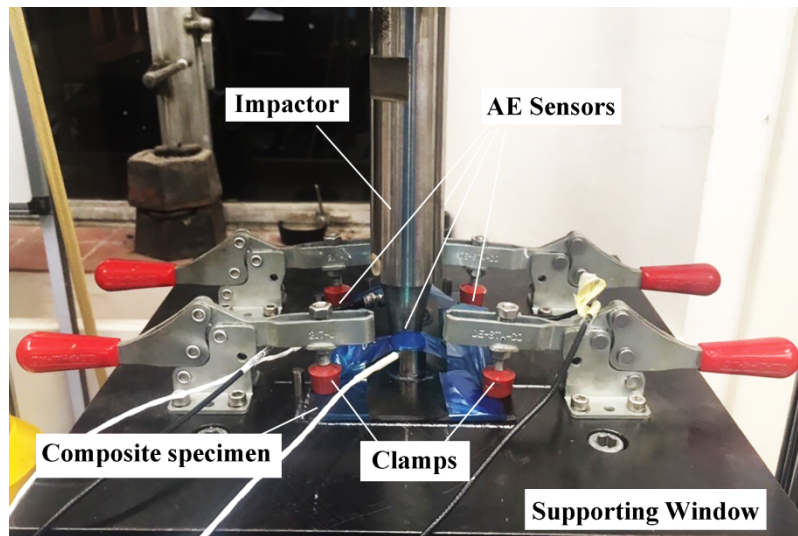
The LVI tests were done according to ASTM D7136 [36] using an INSTRON Dynatup 9250 HV drop-weight impact tower (see Fig. 1.b). The diameter and weight of the impactor are 16 mm and 6.2 kg, respectively. The supporting window and the clamps are the same as the indentation test. The values of acceleration, velocity, deflection, and force were continuously recorded during the tests by the instrumented impact machine. To achieve different impact energies, the impactor was released from various height levels.

Table 2. Configurations of the specimens.

Specimens	Dimensions (mm)	Lay-up	Ply thickness (mm)
S _D	150×100×3	[60/0/-60] _{4s}	0.125
S _B	150×100×3	[60 ₄ /0 ₄ /-60 ₄] _s	0.125



(a)



(b)

Fig. 1. a) Quasi-static indentation, and b) LVI test setups.

2.3. AE system

Four broadband, resonant-type, and single-crystal piezoelectric transducers from Physical Acoustics Corporation (PAC), WD, and the external 40 dB preamplifiers were utilized. The optimum operating frequency range of the AE sensors was [100–900 kHz]. The AE software, AEWIn, and a data acquisition system PAC-PCI-2 with a maximum sampling rate of 40 MHz recorded the AE activities of the specimens. Vacuumed silicon grease was applied between the sensor and specimen surfaces to get an appropriate acoustical coupling between them. The threshold of the receiving AE signals was 40 dB. The pencil lead break procedure was used to calibrate the data acquisition system and ensure a good connection between the specimen surface and the AE sensors [37].

3. The Proposed Methods

In this section, two methods for investigating the evolution behavior of damage in the specimens by AE are proposed; b-value and sentry function methods. These two methods are

widely used in literature to damage assessment in engineering structures. The first one works with the distribution of peak amplitude of AE signals and the second one works with the combination of the mechanical energy and AE energy of the specimens.

3.1. *b*-value

In seismology science, Gutenberg-Richter formula (Eq. 1) is utilized to define the correlation between the intensity and the number of happened earthquakes with the same intensity or more in a specific region [38].

$$\log_{10} N_M = a - bM \quad (1)$$

where M is the reference intensity, N_M is the number of earthquakes with the intensity higher than or equal to M , and a and b are the constants of this equation which are obtained by plotting N_M against M in a logarithmic scale and fitting a line to the data. The slope of the fitted line (b) is named *b*-value. The constants a and b may vary significantly from a region to another region or over time. Due to some similarity between the seismic activities of the earth and AE activities originated from the damage within the material, some researchers have used this method to study the damage evolution in the concrete engineering structures [39-41]. In the context of AE, Gutenberg-Richter formula is modified as follows [39]:

$$\log_{10} N_{A_{dB}} = a - b\left(\frac{A_{dB}}{20}\right) \quad (2)$$

where A_{dB} is the amplitude of AE events in dB scale, $N_{A_{dB}}$ is the number of AE events with the amplitude higher than or equal to A_{dB} , a is a constant and b is the *b*-value parameter. The *b*-value shows the proportion of the low amplitude to high amplitude AE events. A large *b*-value expresses that most AE events have low amplitude that is a sign of micro damages in the

material and a low b-value illustrates the higher content of the high amplitude AE events against the low amplitude AE events that is a sign of macro damages in the material [40-41].

The drawback of b-value method is that it works with the peak amplitude of AE signals while the peak amplitude is highly affected by some phenomena during the propagation of the wave such as attenuation, scattering, refraction, reflection, etc. However, the energy of AE signals (the integration of amplitude over the time) seems to be a better parameter that shows the average intensity of the wave and it is less sensitive to the propagation phenomena.

3.2. Sentry function

Sentry function ($f(x)$) is defined as the logarithm of mechanical energy to AE energy [42]:

$$f(x) = \ln \left[\frac{E_m(x)}{E_a(x)} \right] \quad (3)$$

where $E_m(x)$, $E_a(x)$ and x are the mechanical energy (area beneath the load-displacement curve), the cumulative AE energy and the displacement, respectively.

According to the state of damage in the material this function illustrates four different trends:

- 1) Increasing trend (S1): it expresses that some scattered micro damages are happening in the material, but they cannot considerably degrade the integrity of the structure.
- 2) Sharp drop (S2): the continuous generation of micro damages in composite materials usually leads to the accumulation and coalescence of micro damages and consequently results in the occurring of a significant macro damage. This macro damage associates with a sharp drop in the sentry function curve.
- 3) Gradually decreasing trend (S3): this trend is usually seen when the macro and micro damages significantly degrade the integrity of the material and the material is continuously losing its load-bearing capability.
- 4) Constant trend (S4): it shows that there is a semi-balance

state between the degrading mechanisms such as damage mechanisms and some stiffening mechanisms such as fiber bridging in the composite materials.

The advantages of sentry function against b-value are that the sentry function uses the AE energy instead of the peak amplitude and also it employs the mechanical energy in addition to the AE energy that it leads to more sensitivity of the sentry function to damage in the material.

3.3. Wavelet packet transform

WPT is defined as the decomposition of a signal into the low-frequency part, approximation, and the high-frequency part, detail. In the next decomposition level, each component splits into new approximation and detail. This procedure is continued until reaching the desired decomposition level that usually is obtained by entropy criterion (see Fig. 2). Each component in WPT tree has a specific frequency content associated with its position in the tree. The frequency content of each component is calculated using Eq. 4 [43]:

$$[nf_s 2^{-(i+1)}, (n+1)f_s 2^{-(i+1)}] \quad (4)$$

where f_s is the sampling rate, i is the decomposition level index, and n shows the components number that is equal to $n=0, 1, \dots, 2^{i-1}$ for decomposition level i . More information about the theory of WPT can be found in literature [43- 45].

The energy of each component in decomposition level i (E_i^n) is calculated by Eq. 5:

$$E_i^n = \sum_{T=t_0^n}^{t_1^n} [f_i^n(T)]^2 \quad (5)$$

where f_i^n is the WPT component and t_0^n and t_1^n show its time period. The energy percentage of each component in the total energy of the original signal is calculated by Eq. 6:

$$P_i^n = \frac{E_i^n}{\sum_i \sum_n E_i^n} \quad (6)$$

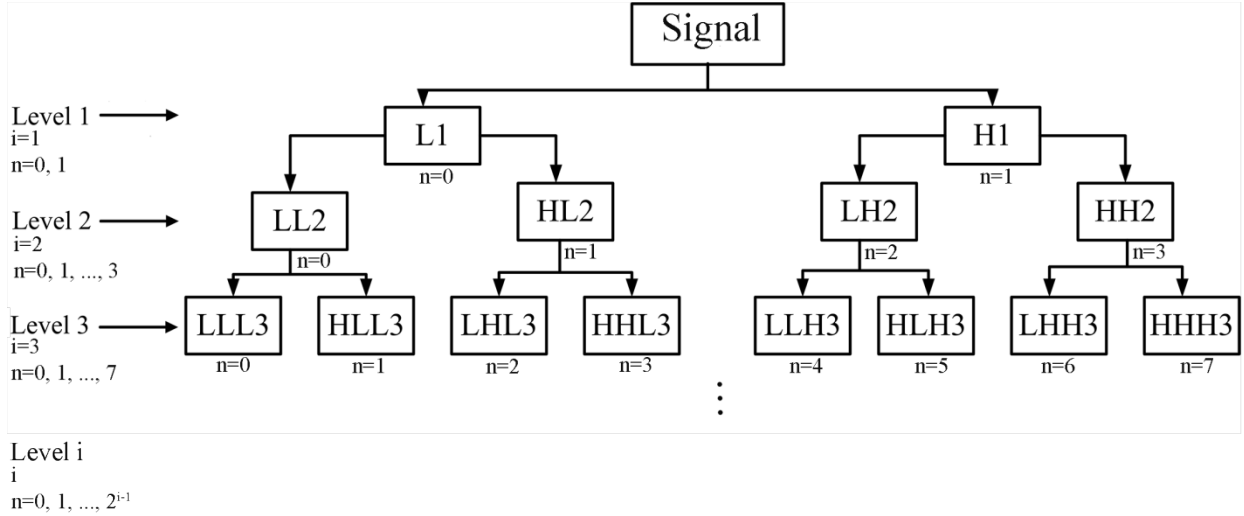


Fig. 2. A schematic of the WPT tree (L: low frequency part (approximation), and H: high frequency part (detail)).

4. Results and Discussions

The results are presented in two sections. The first section is devoted to the study of BVID in quasi-static indentation loading and in the second section, the BVID of the specimens under LVI loading condition is represented.

4.1. Quasi-static indentation test

The load-displacement curves and also the C-scan images of the specimens under quasi-static indentation loading are shown in Fig. 3. The load curve of specimen S_D increases linearly to 3 kN where it experiences a sharp drop. Then, it increases with a lower gradient until load 7.8 kN where the final fracture occurs. The load curve of specimen S_B has a different trend. It increases linearly from the beginning of the test to load 1.3 kN where a considerable reduction in the

stiffness of the specimen is seen. Then, the load increases with a lower gradient to load 4 kN where a sharp drop is observed in the curve and it is then followed by some unstable load increasing trends until load 4.9 kN where the final fracture occurs. In order to better explain the evolution behavior of BVID in quasi-static indentation, some C-scan and digital camera images were taken from the indented surface and cross-section of the midplane of the specimens at different load levels (see Figs. 3 and 4). To this aim, 5 coupons from each layup were fabricated and subjected to the following tests: a) 3 coupons were loaded to the final fracture to check the repeatability of the test and also to specify the location of the load drops, b) 1 coupon was loaded until just after the first load drop, and c) 1 coupon was loaded until just before the first load drop. Accordingly, the BVID evolution is studied at three different stages; 1) the linear elastic region of the load curve, 2) a little after the end of the elastic region, and 3) the final fracture. According to Fig. 3, the C-scan images do not show any delamination in both specimens in the linear elastic region while the taken C-scan images after the elastic region show the presence of some delaminated regions in both specimens. Although the maximum area of delamination for specimen S_B is much bigger than S_D , the digital images of the cross-section show that the number of delaminated interfaces for specimen S_D is higher than S_B . The higher number of delaminated interfaces in specimen S_D in comparison to S_B is due to the higher number of dissimilar interfaces in this specimen and also the bigger area of delaminated region in specimen S_B is due to the higher value of interfacial shear stress at the dissimilar interfaces of this specimen in comparison to S_D [46]. The digital images also show more transverse matrix cracks in both specimens in this region. The C-scan images at the final fracture show the considerable growth of delamination, especially for specimen S_B that is due to the higher interfacial shear stress in this specimen. The digital images also show that the number of delaminated interfaces for specimen S_D increases from 7 at the end of the elastic region to 19 at the final fracture and in

the case of specimen S_B the number of delaminated interfaces increases from 2 at the end of the elastic region to 4 at the final fracture. The amount of transverse matrix cracks also increases considerably for both specimens. Also, the digital images of the cross-section illustrate that the BVID in specimen S_D is almost locally that shows the dominant loading mode in this specimen is penetration, while the BVID in specimen S_B is nonlocal that illustrates the dominant loading mode in this specimen is bending.

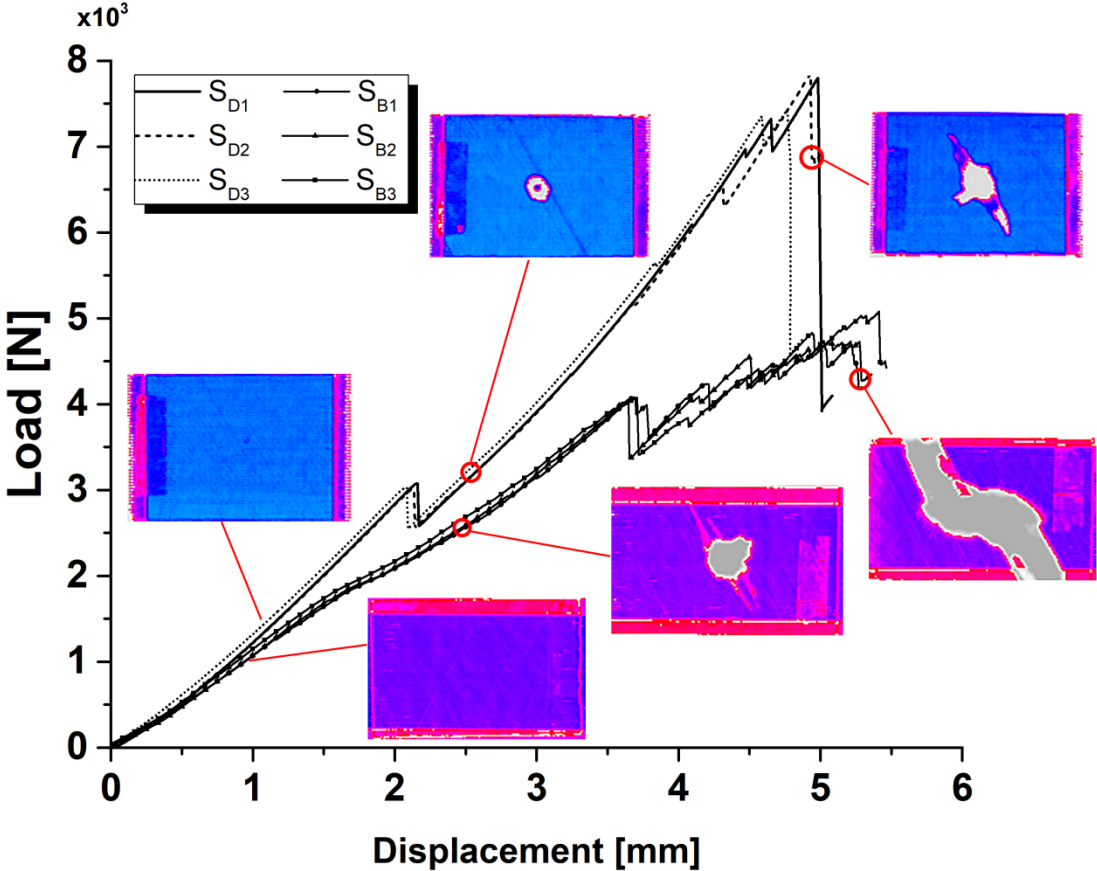


Fig. 3. The load-displacement curve of the specimens and the ultrasonic C-scan images at different stages of loading.

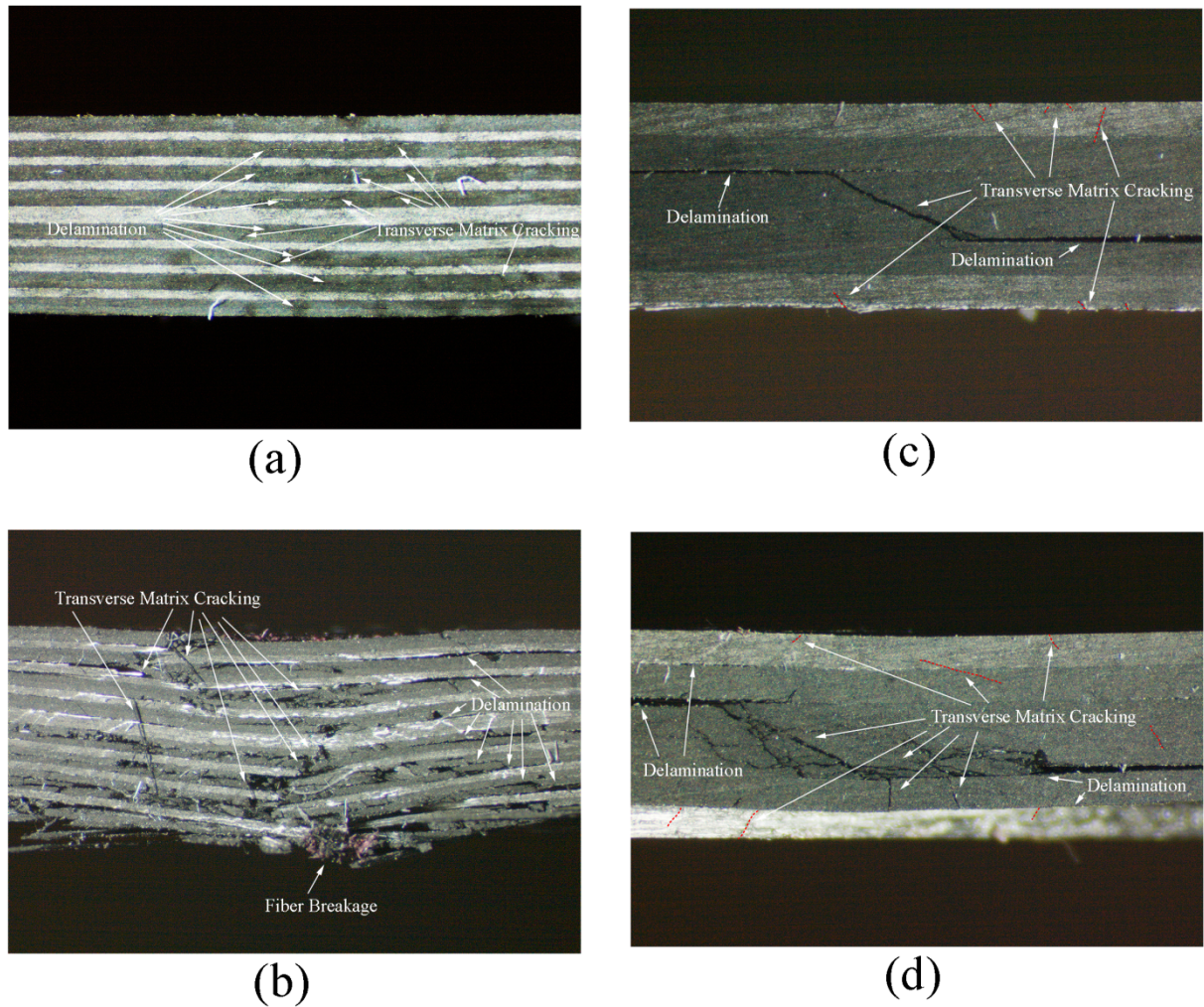


Fig. 4. A cross-section overview of midplane of the longitudinal direction for a) S_D -after the elastic region, b) S_D -final fracture, c) S_B - after the elastic region, d) S_B -final fracture [32].

In our previous research [32], the performance of six different clustering methods to classify the AE signals of interlaminar and intralaminar damage mechanisms in specimens S_D and S_B under quasi-static indentation loading is compared and finally, three damage mechanisms containing matrix cracking, fiber breakage and delamination were clustered using the hierarchical model. The clustered AE data of these damage mechanisms is shown in Fig. 5.

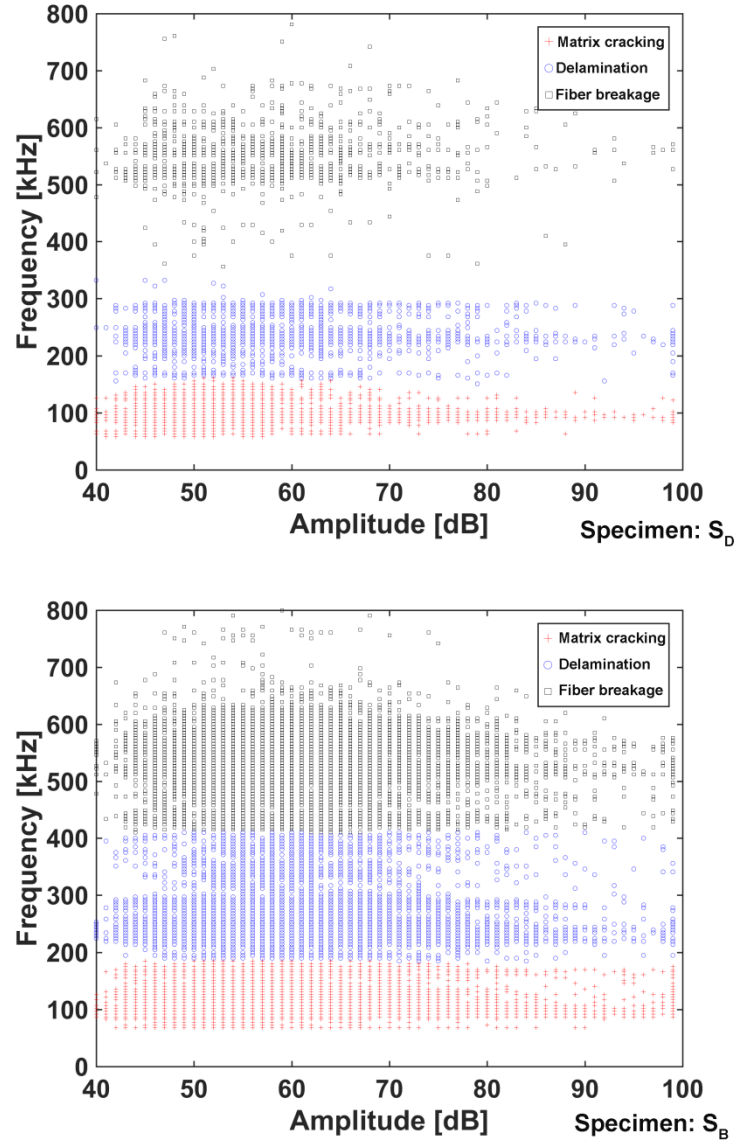


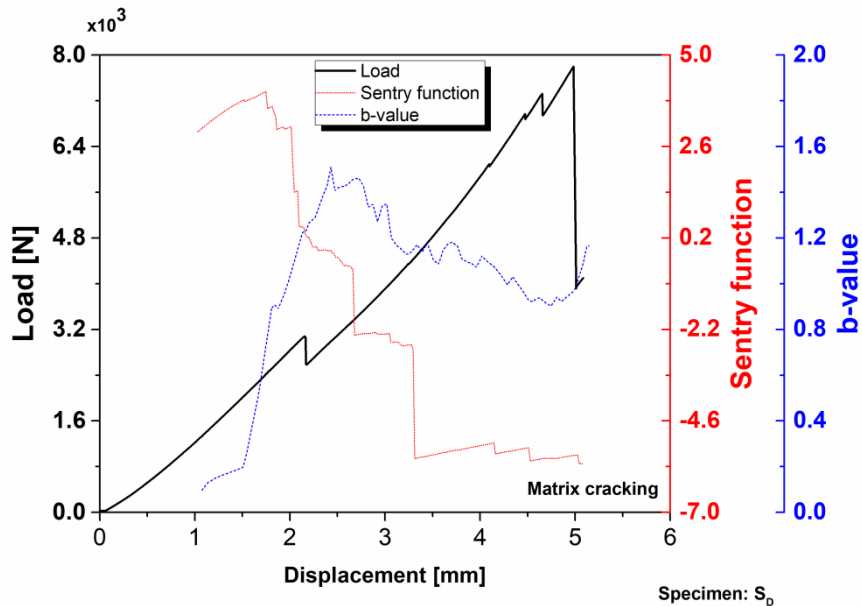
Fig. 5. The clustered AE data of different damage mechanisms in the quasi-static indentation tests [32].

In the present study, the evolution behavior of each damage mechanism is completely analyzed using the b-value and sentry function methods and the performance of these two methods to track the evolution behavior of BVID is compared with each other. To this aim, the sentry function and b-value methods were employed to analyze the data of each cluster in Fig. 5, separately. The b-value and sentry function curves of matrix cracking, delamination, and fiber breakage for specimens S_D and S_B are shown in Figs. 6-8. The behavior of the curves is

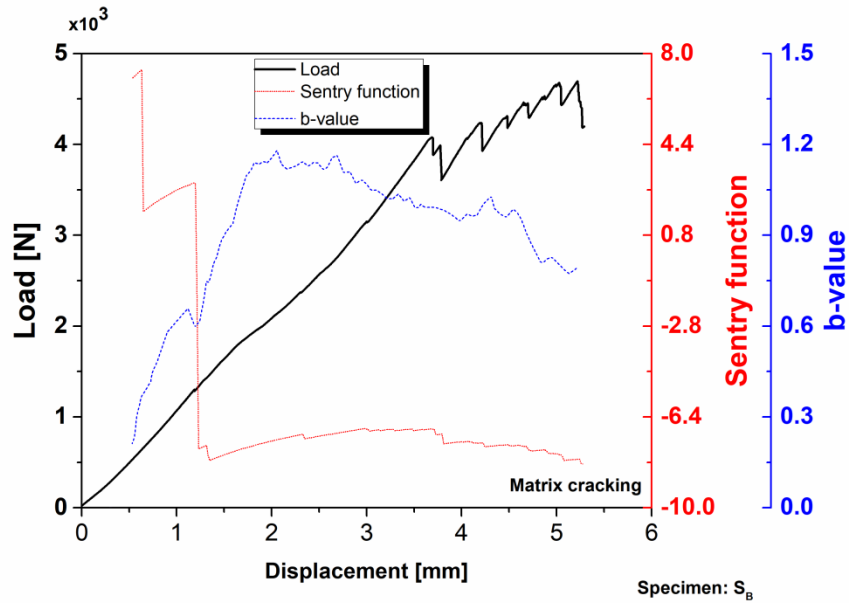
investigated in two regions, the initial elastic region, and after the elastic region to the final fracture. Fig. 6 shows the b-value and sentry function curves of matrix cracking. According to Fig. 6.a, the sentry function curve of specimen S_D shows an increasing trend at first that its gradient is gradually reduced. This fact illustrates that some micro matrix cracks are occurring within the specimen, but they don't significantly degrade the global stiffness of the specimen. Then, some small drops are seen just before the first significant load drop which are then followed by a significant drop at the moment of load drop. This behavior shows the accumulation and coalescence of micro matrix cracks that lead to a significant macro matrix damage. After this sharp dropping, the sentry function curve experiences some gradually decreasing trends that each one is followed by a sharp drop until the final fracture. This behavior is a sign of the gradual evolution of old matrix cracks (S3) and occurring of new matrix cracks (S2), simultaneously. The general behavior of b-value curve of specimen S_D is in accordance with the sentry function but it has a time delay to response to damage. The b-value has an increasing trend in the linear elastic region which shows occurring of some micro matrix cracks, but no significant change in b-value curve is seen at the moment of load drop. Then, shortly after the first load drop, b-value curve is undergone some consequently drops until the final fracture that these drops are the sign of unstable and macroscopic matrix damage evolution.

As is shown in Fig. 6.b, in the case of specimen S_B , the sentry function curve of matrix cracking has an increasing trend at first which is then followed by two very big drops, the first one before and the second one at the moment of stiffness degradation point. Then it shows some increasing trends with the infinitesimal gradients that they illustrate the occurring of micro matrix cracks. It then experiences a gradually decreasing trend around load 4 kN that exhibits the structure is losing its load-bearing capability. The b-value curve shows an increasing trend at first which is followed by a significant drop at the moment of stiffness degradation. Then, it

increases to its maximum value where it is approximately has a constant behavior or very gradually decreasing trend that is a sign of micro matrix crack occurrence. It also experiences some significant drops after load 4 kN which show the occurring of macro matrix cracks. As can be seen in Fig. 6.b, the b-value could not get the first drop in the Sentry function curve. This is due to the fact that b-value works with the peak amplitude distribution of an AE data batch over a time period and by this manner the effect of one high-intensity AE signal inside the data batch is reduced. While Sentry function works with the individual AE data and thus it is sensitive to the individual high energy AE signal. The behavior of the b-value and Sentry function shows that the matrix cracking evolution in specimen S_D is unstable while the evolution of matrix cracking in specimen S_B has a more stable behavior.



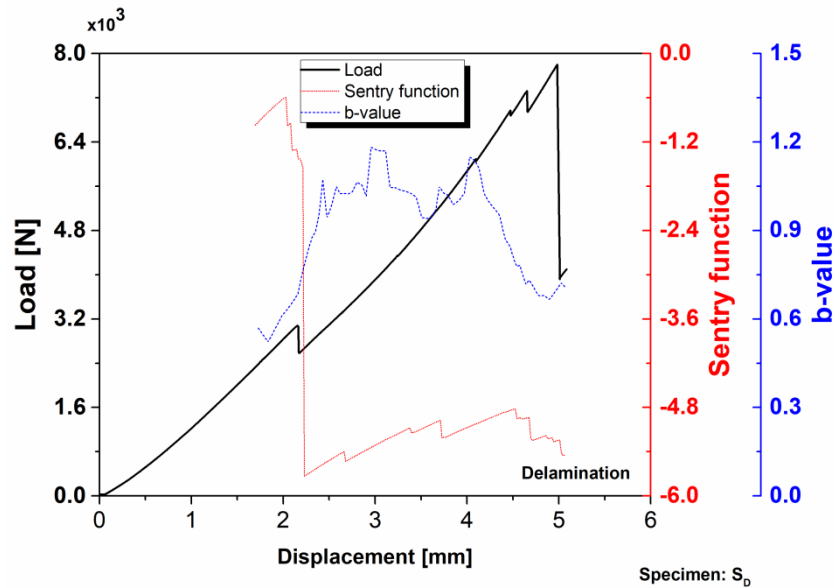
(a)



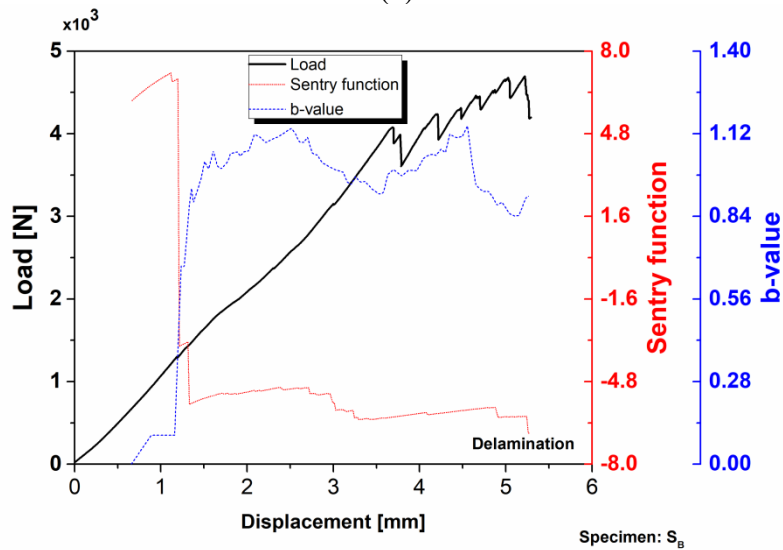
(b)

Fig. 6. The b-value and sentry function curves of matrix cracking for specimen a) S_D and b) S_B .

Fig. 7 illustrates the b-value and sentry function curves of delamination for specimens S_D and S_B . According to Fig. 7.a, for specimen S_D , the b-value and sentry function show an increasing trend before the first load drop. This behavior demonstrates the occurring of some infinitesimal delaminations. Then, the sentry function curve experiences a significant drop at the moment of load drop that it is a sign of considerable delamination growth at this point while b-value curve detects the occurring of delamination at the first load drop with a time delay (the first drop in b-value curve shortly after the first load drop). Afterward, the sentry function shows some increasing trends that each one is followed by a drop that it may be related to the occurring of new delaminations at some interfaces. The b-value curve also illustrates some increasing trends that each one is followed by a drop. As seen in Fig. 7.b, the sentry function and b-value curves for specimen S_B have more stable behavior. This is due to the lower number of dissimilar interfaces that are susceptible to delamination in this specimen.



(a)



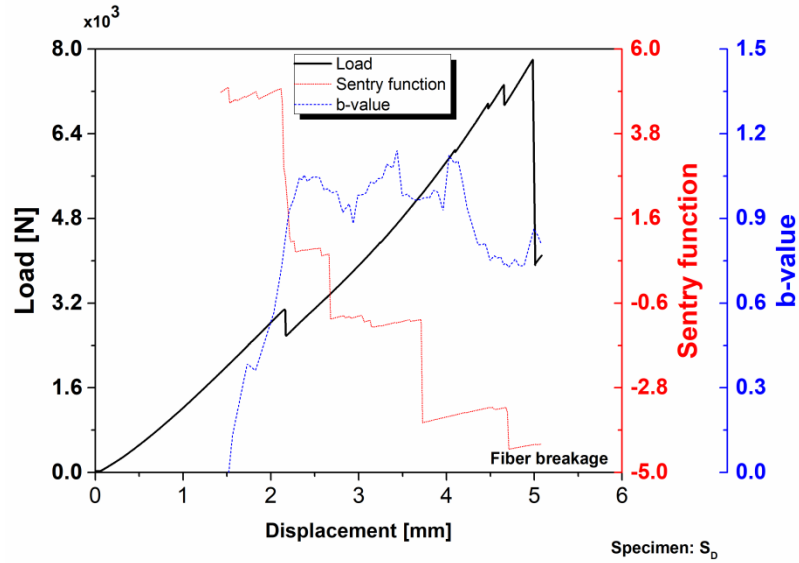
(b)

Fig. 7. The b-value and sentry function curves of delamination for specimen a) S_D and b) S_B .

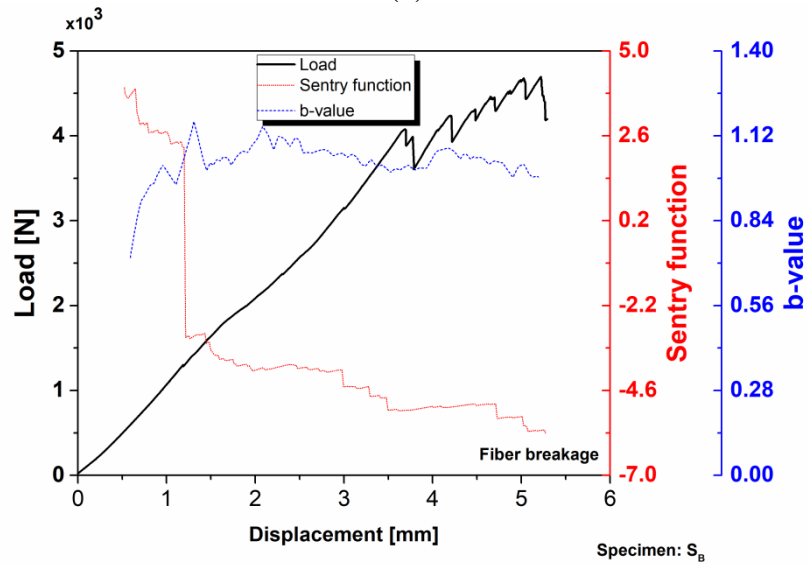
The sentry function and b-value curves of fiber breakage for specimens S_D and S_B are shown in Fig. 8. In the case of specimen S_D (see Fig. 8.a), both b-value and sentry function have an increasing trend at first. The sentry function is then continued by a step-by-step dropping behavior which is a sign of unstable fiber breakage. Wherever the sentry function has a constant trend (S4), micro fiber breakage occurs while at the sharp dropping points (S2) bundle fiber

breakage occurs. The b-value curve has a similar trend with the sentry function but with a time delay. For specimen S_B (see Fig. 8.b), the sentry function shows a gradually decreasing trend at first that shows some considerable micro fiber breakages occur in the specimen. Then, it is followed by a big drop which is related to the fiber bundle fracture. After this drop, sentry function is almost constant and only some small drops are seen which are due to some macro fiber breakages. The b-value curve has an increasing trend at first which shows the dominant damage mode in this stage is micro fiber failure. It is then followed by a small drop at the end of the elastic region which is a sign of fracture of a fiber bundle. Then, the b-value curve shows a constant behavior until the final fracture that illustrates the occurring of micro fiber breakage in this region. These are in accordance with the cross-section overviews of the specimens (see Fig. 4). As can be seen in Fig. 4, the dominant loading mode in specimen S_D is penetration. Therefore, when the indenter wants to penetrate into the specimen, it breaks fiber layers to penetrate into the laminate. Thus, breaking of each fiber layer produces a significant drop in the sentry function and b-value curves. While, in the case of the blocked specimen (S_B), the dominant loading mode is bending. Thus only some scatter fiber breakages occur in the specimen and consequently a semi-constant behavior for sentry function and b-value curves is seen.

Finally, by comparing the behavior of the sentry function and b-value curves for the damage mechanisms, it is found that although both methods could detect the general behavior of damages evolution, the sentry function is more sensitive to damage and also detects the induced damages sooner than the b-value method.



(a)



(b)

Fig. 8. The b-value and sentry function curves of fiber breakage for specimen a) S_D and b) S_B .

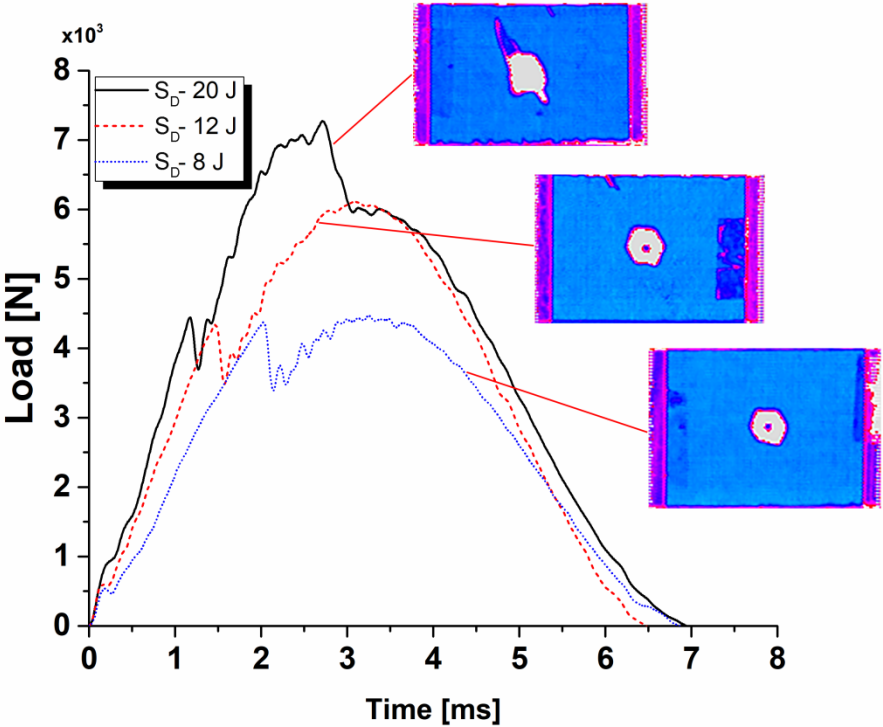
4.2. Low-velocity impact tests

The LVI tests were conducted using the obtained information from the indentation tests. Three different energy levels consisting of 8 J, 12 J, and 20 J were selected for the impact tests. It was expected that the lowest energy induces a load more than the maximum load at the linear elastic region of the indentation load curve and the highest energy makes a load close to the final fracture load and finally, the middle energy induces a load between these two values. The load-

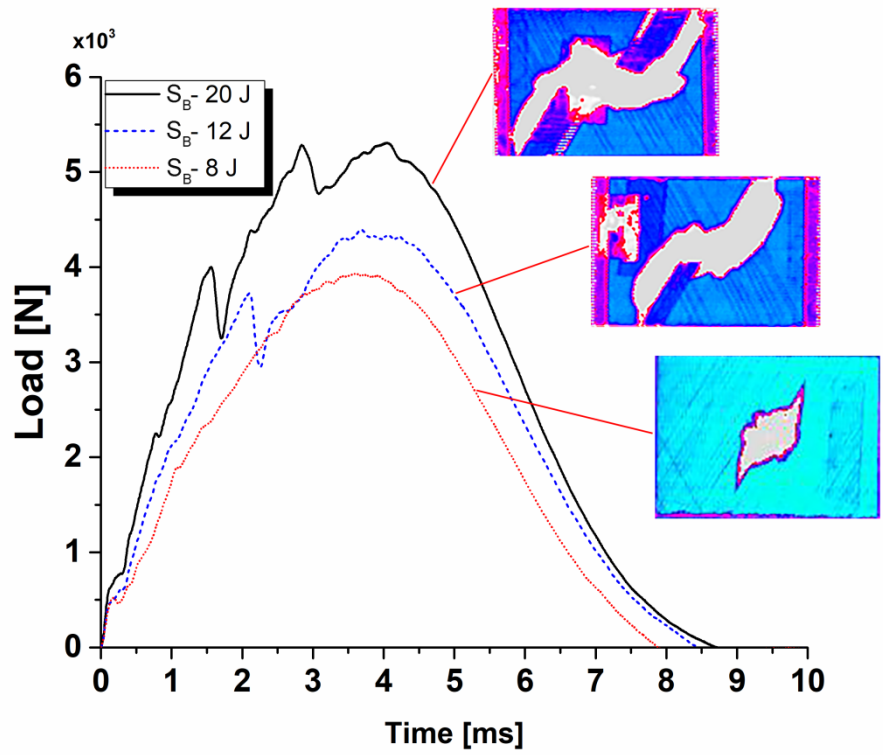
time curves and also the C-scan images of the impacted specimens are shown in Fig. 9. According to Fig. 9, the load curve of all three impacts for specimen S_D increases to load 4.2 kN, where a significant drop occurs in the load curve. This may relate to the delamination initiation and unstable growth in the specimens. The load falling is then followed by a load increasing trend. The increasing trend of impacts 8 J and 12 J is different from impact 20 J. Due to the lower energy of impacts 8 J and 12 J, they cannot induce new delamination in the specimen and their load curve reaches the maximum value and then gradually decreases to zero. On the other hand, due to the higher energy of impact 20 J, its load curve increases until load 7.2 kN where the second delamination unstable growth occurs in the specimen. The C-scan images of the impacted specimens confirm this claim. As can be seen in Fig. 9.a, the delamination area of impacts 8 J and 12 J are almost the same and they are smaller than the delamination area of impact 20 J. In the case of specimen S_B , the load curve of all three impacts increases to load 2.1 kN where a small stiffness reduction in the load curve is observed. The load curve of impact 8 J then increases to its maximum value without inducing a new delamination in the specimen and consequently, it gradually decreases to zero. However, the load curve of impacts 12 J and 20 J increases after the stiffness reduction point until load 4 kN where another significant drop occurs which is associated with the new delamination initiation and unstable growth. After this load drop, the load of impact 12 J reaches to the maximum value and gradually decreases without generating new delamination, while the load curve of impact 20 J experiences another drop around load 5.5 kN that shows the inducing of new damages in the specimen. The increasing of delamination area in C-scan images of impacts 8 J to 20 J confirms this claim (see Fig. 9.b).

Fig. 10 shows the digital camera images from the cross-section of the midplane of the impacted specimens. Some small delaminated interfaces and transverse matrix cracks are seen in specimen S_D subjected to impact 8 J. By increasing the impact energy to 12 J, no new

delaminated interface is seen in the specimen and only the amount of transverse matrix cracks is increased. While the image of impact 20 J shows some new delaminations and transverse matrix cracks in specimen S_D . These results are consistent with the C-scan results and load-time diagrams of specimen S_D . The digital camera image of specimen S_B subjected to impact 8 J illustrates 3 delaminated interfaces and some transverse matrix cracks. The number of delaminated interfaces is increased to 4 and the density of transverse matrix cracks is increased for impact 12 J. The image of impact 20 J shows 4 severe delaminated interfaces and much more transverse matrix cracks for the specimen. These results have a good consistency with the C-scan images and load-time diagrams of specimen S_B .

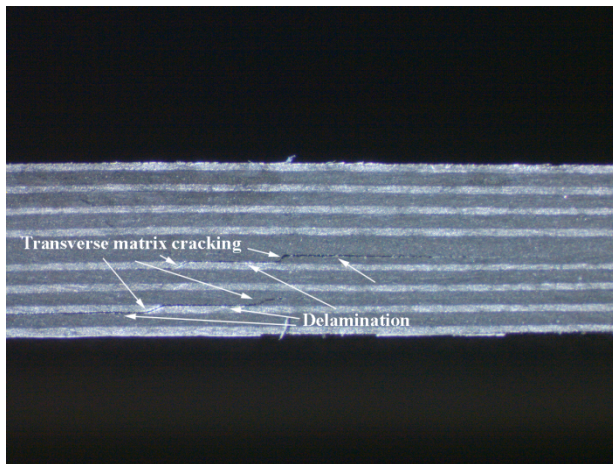


(a)

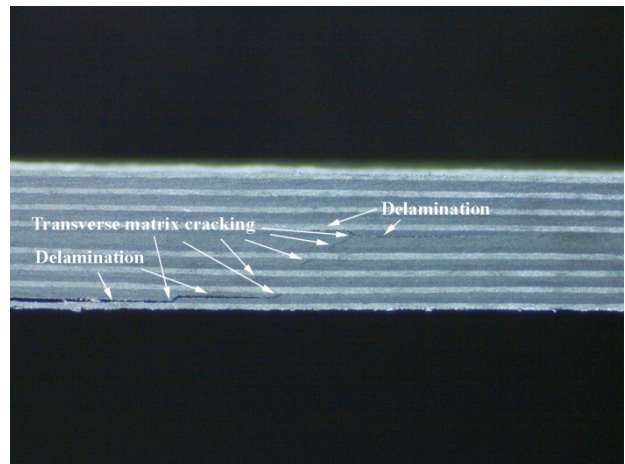


(b)

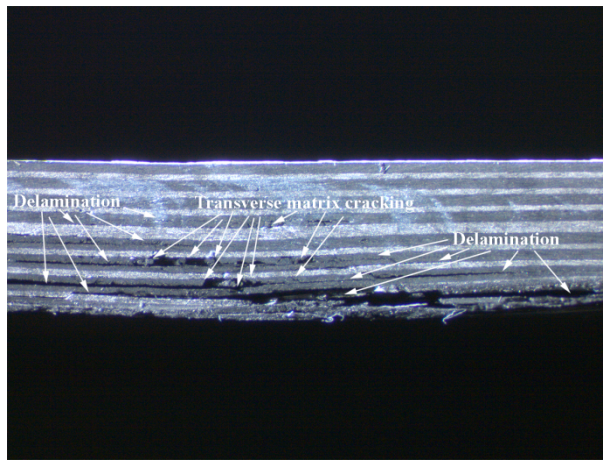
Fig. 9. The load-time curve and the ultrasonic C-scan images of impact tests for specimen a) S_D , and b) S_B .



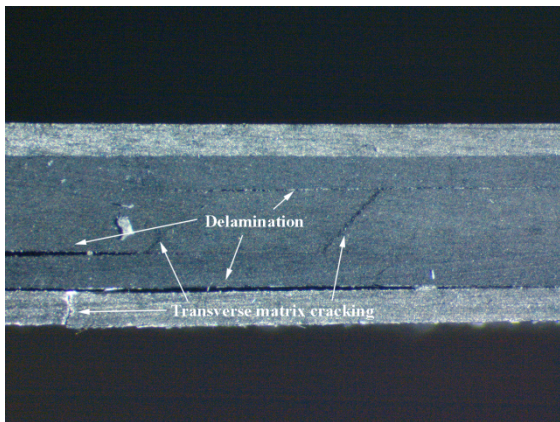
(a)



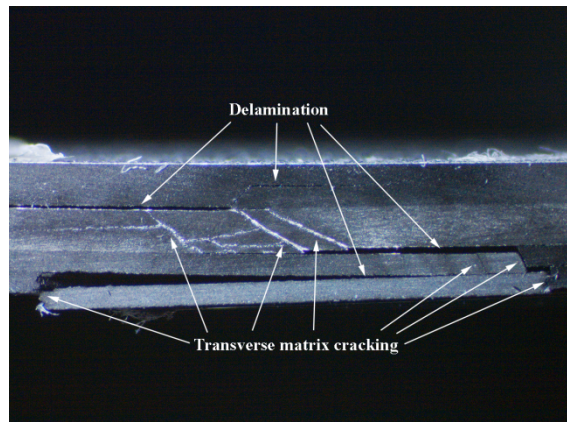
(b)



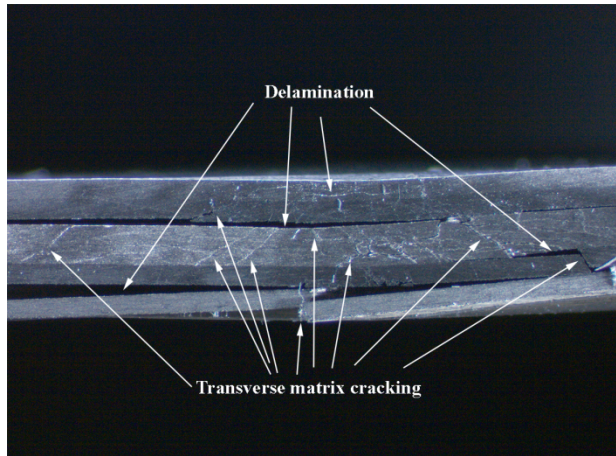
(c)



(d)



(e)



(f)

Fig.10. A cross-section overview of midplane of the impacted specimens, a) $S_D-8 J$, b) $S_D-12 J$, c) $S_D-20 J$, d) $S_B-8 J$, e) $S_B-12 J$, f) $S_B-20 J$.

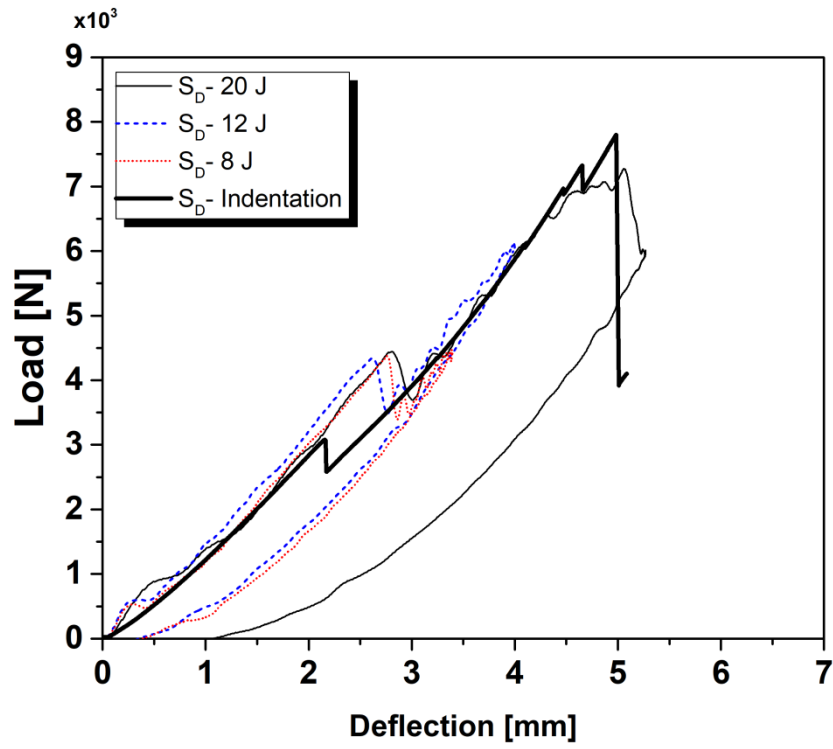
In order to provide a better comparison between the behavior of the specimens under LVI and quasi-static indentation loading conditions, the load-deflection curves of the LVI tests are plotted

against the load curve of quasi-static indentation tests (see Fig. 11). As can be seen in Fig. 11, the flexural rigidities of the load curves for LVI and indentation tests are the same. This fact shows the accuracy of recorded displacement and force during the indentation and LVI tests. However, there is a significant increase in the critical load corresponded to the initial delamination growth for the LVI tests in compared with the indentation tests. The amount of this increase is reported in Table 3. According to literature [47], the corresponding load to first delamination growth in a laminated composite under an out-of-plane load ($F_{Delamination}$) is proportional to the laminate stiffness (E_{eq}), laminate thickness (h), and mode II interlaminar fracture toughness (G_{IIC}):

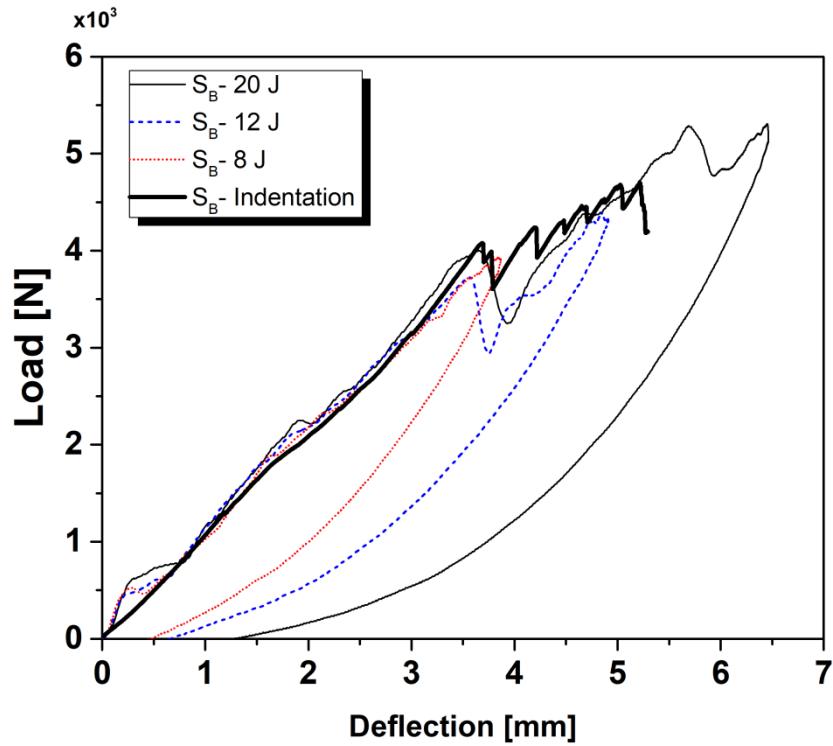
$$F_{Delamination} = \left[\frac{32\pi^2 D G_{IIC}}{3} \right]^{\frac{1}{2}} \quad (5)$$

where $D = \frac{E_{eq} h^3}{12(1-\nu^2)}$ is the equivalent bending stiffness.

The laminate thickness for both quasi-static indentation and LVI specimens is equal and also according to Fig. 11, the stiffness of both indentation and LVI tests is the same. Thus, the only parameter that may increase the critical load in LVI tests is the increasing of G_{IIC} under high loading rates, although according to authors' knowledge, the effect of loading rate on G_{IIC} is not investigated in literature yet.



(a)



(b)

Fig. 11. The load- deflection curves of LVI and indentation tests for specimen a) S_D , and b) S_B .

Table 3. The corresponded load to the initial delamination growth in indentation and LVI tests.

Specimen	The corresponded load to the initial delamination growth (critical load) (kN)			Critical load increasing under LVI in compared with indentation (%)	
	Indentation	LVI			
		8 J	12 J		20 J
S _D	3.07	4.38	4.33	4.43	42.67
S _B	1.30	1.86	2.07	2.24	58.21

In order to compare the induced delamination under quasi-static indentation and impact 20 J tests, area of the delaminated region for the indentation and impact 20 J specimens was calculated using the image processing of the C-scan images represented in Figs. 3 and 9 and it is reported in Table 4. As can be seen in Figs. 3 and 9 and Table 4, the shape and area of the delaminated region for the quasi-static indentation and impact 20 J tests have a good consistency with each other and the maximum difference of the delaminated area is about 10%. The smaller area of the delaminated region for LVI tests against the indentation tests is due to the increasing of G_{IIC} under high loading rates.

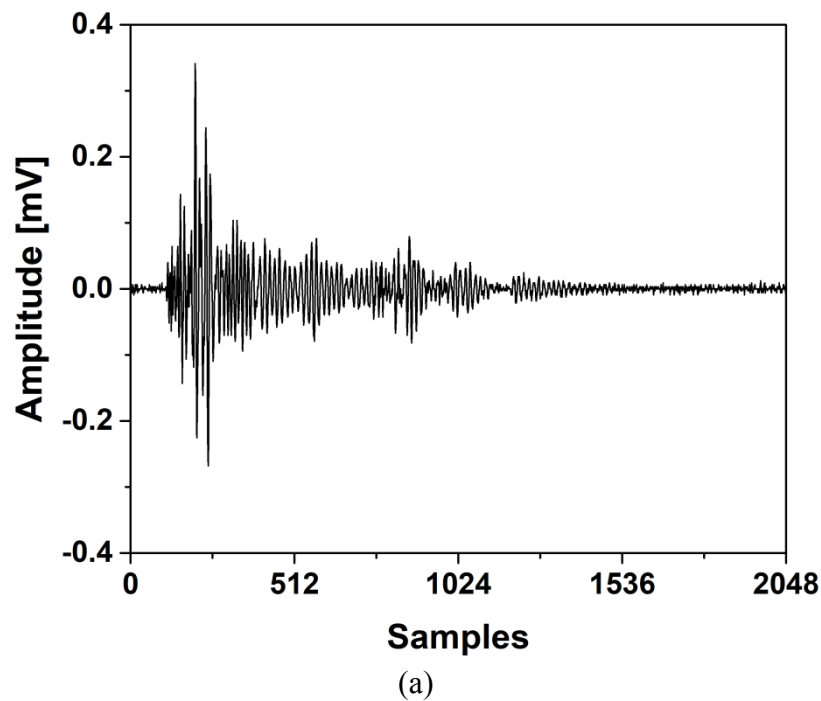
Therefore, although the general behavior of the specimens under quasi-static indentation and LVI tests has a considerable similarity, there are two differences that should be considered if the quasi-static indentation test is taken instead of LVI test to better investigation of BVID; the higher critical load and lower area of the delaminated region in LVI test in comparison to quasi-static indentation test.

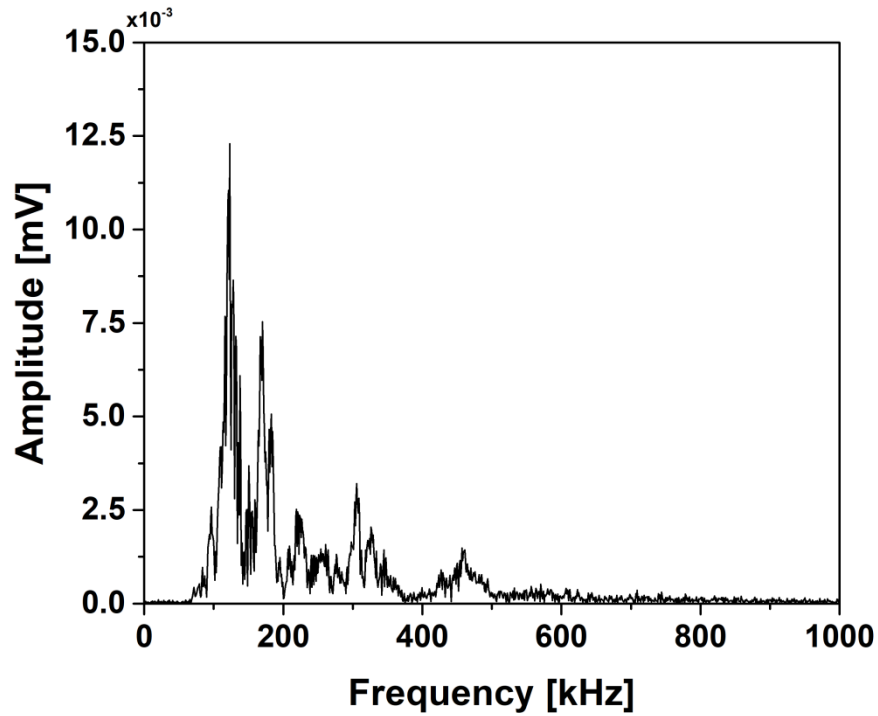
Table 4. Area of the delaminated region for the indentation and impact tests' specimens.

Specimen	Area of the delaminated region (mm ²)		Difference between the delaminated area of indentation and impact 20 J tests (%)
	Indentation (at final fracture point)	LVI (20 J)	
S _D	556.5	545.0	2.1

S_B	3847.4	3446.1	10.4
-------	--------	--------	------

Fig. 12 shows a recorded AE waveform during the impact test of the specimens and its Fast Furrier Transform (FFT). As can be seen in Fig. 12.b, there are three main frequency contents in the frequency distribution of the AE signal consisting of [60-150 kHz], [150- 375 kHz], and above 375 kHz. These frequency contents are in accordance with the frequency contents of matrix cracking, delamination, and fiber breakage in the indentation tests, respectively (see Fig. 5). Thus, it is found that during the impact test, due to the short time of the loading, the AE signals of different damage mechanisms interfere with each other and one recorded AE waveform may have three different damage mechanisms inside itself. Thus, in order to identify the percentage of different damage mechanisms during the impact loading, the recorded AE signals are analyzed by WPT method and finally, energy criterion is employed to determine the amount of energy for each damage mechanism in the original AE signals.

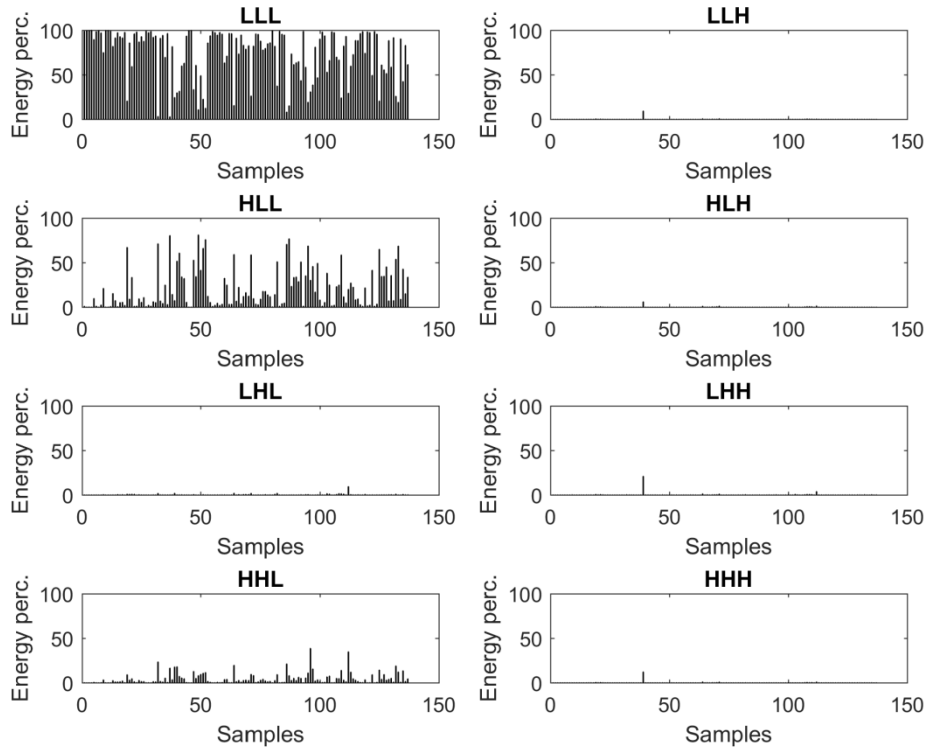




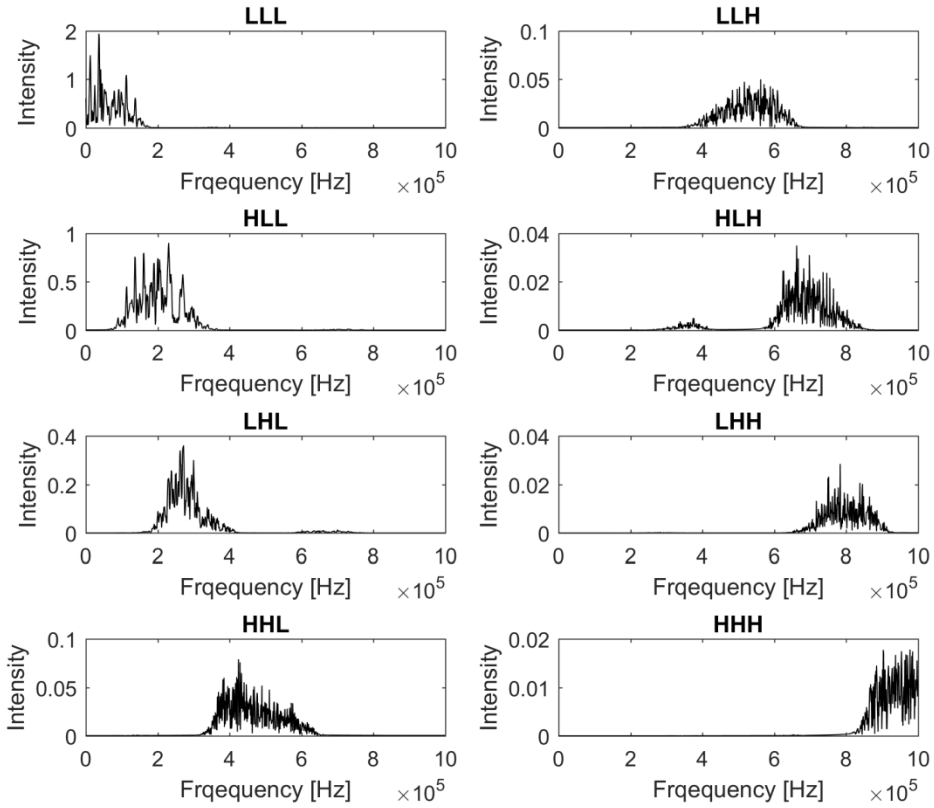
(b)

Fig. 12. a) An AE waveform recorded during the impact test, and b) the frequency distribution of the AE signal obtained by FFT.

The AE signals of impact tests are decomposed into three levels (the best decomposition level was obtained by entropy criterion) and 8 components by Daubechies 10 wavelet that is frequently used for AE signals analysis. The energy and frequency contents of each component of the decomposed AE signals for specimen S_B under impact 20 J are shown in Fig. 13. The frequency content of each component was obtained by FFT.



(a)



(b)

Fig. 13. a) The energy content, and b) the frequency content for each WPT component of the decomposed AE signals of specimen S_B under impact 20 J.

According to the frequency distribution of WPT components (see Fig. 13.b) and the frequency content of the damage mechanisms (see Fig. 5), it is found that component LLL, with the frequency content less than 200 kHz, associates with matrix cracking, components HLL and LHL, with the general frequency content of [150-400 kHz] are related to delamination, and components HHL and LLH with the general frequency content of [350-650 kHz] associate with fiber breakage. The energy percentages of these three damage mechanisms are then calculated using the energy criterion (Eq. 6) and they are reported in Table 5. As can be seen, for specimen S_D under impact 8 J, the dominant damage mode is matrix cracking. By increasing the impact energy to 12 J, the percentage of matrix cracking increases and the percentage of delamination decreases. In accordance with the C-scan images of impacts 8 J and 12 J on specimen S_D (see Fig. 9.a), the delaminated area of impacts 8 J and 12 J is equal. Thus, it is concluded that the additional energy of impact 12 J is devoted to make new matrix cracking and fiber breakage. Therefore, the percentage of matrix cracking and fiber breakage increases and the percentage of delamination decreases. According to C-scan image of specimen S_D under impact 20 J, it is obvious that the delaminated area increases significantly. Thus, the most of the additional energy of impact 20 J in comparison to impact 12 J, is spent for delamination initiation and propagation. Therefore, by increasing the energy of impact from 12 J to 20 J, the percentage of delamination increases and the percentage of matrix cracking decreases. Also, due to higher energy of impact 20 J, some new fiber breakages occur in the specimen and the percentage of fiber breakage does not decrease. In the case of specimen S_B under impact 8 J, although the dominant damage mechanism is matrix cracking, the AE data shows the higher percentage of delamination in comparison to specimen S_D , which is consistent with the bigger area of delamination for this specimen. Also, by increasing the energy of impact to 12 J, the amount of matrix cracking increases significantly and delamination decreases. Although the delamination area of impact 12

J is bigger than impact 8 J for specimen S_B, however, the AE data shows that the bigger part of the additional impact energy is devoted to make matrix cracking and a smaller portion of the impact energy is dedicated to make new delamination. It is expectable because the dissimilar interfaces of specimen S_B are only 4 that it shows there is a limit on the initiation of new delamination. Thus, more portion of additional impact energy is spent on making new matrix cracking. By increasing the energy of impact from 12 J to 20 J, there is no considerable change in the damages percentage. This fact shows that there is an equilibrium state among the damage mechanisms in the specimen.

Finally, in order to compare the percentage of different damage mechanisms in LVI tests with the indentation tests, the percentage of different damage mechanisms for impact 20 J tests be compared with the quasi-static indentation test results (see Table 5). As can be seen, despite the dynamic and quasi-static nature of LVI and indentation tests and also the utilized method (clustering indentation AE data by hierarchical model [32] and analyzing impact data by WPT) there is a good consistency between the percentage of different damage mechanisms for LVI and indentation tests that it shows AE is a powerful tool to monitor BVID in laminated composite structures under different loading conditions.

Table 5. The energy percentage of interlaminar and intralaminar damage mechanisms in the LVI specimens obtained from WPT and energy criterion.

Specimen	Impact Energy (J)	Damage mechanisms			Reference
		Matrix cracking	Delamination	Fiber breakage	
S _D	8	64.4%	27.2%	4.9%	-
	12	71.5%	18.0%	9.0%	-
	20	65.3%	23.4%	9.1%	-
	Indentation	50.3%	38%	11.7%	[32]
S _B	8	42.0%	36.0%	20.4%	-
	12	73.0%	20.3%	6.4%	-
	20	73.8%	20.8%	4.6%	-

Indentation	77.1%	16.5%	6.4%	[32]
-------------	-------	-------	------	------

Note: Due to the fact that a few percent of the energy of the AE signals is devoted to the WPT components with the frequency higher than 650 kHz (see Fig. 13), the summation of the percentage of damage mechanisms for LVI tests is not 100%.

5. Conclusion

This study focused on the assessment of BVID in carbon/epoxy laminated composites by AE. To this aim, two quasi-isotropic specimens with the layups of $[60/0/-60]_{4S}$ and $[60_4/0_4/-60_4]_S$ were fabricated and subjected to the quasi-static indentation loading. The load- displacement curves and also C-scan and digital camera images were employed to comprehensive study of BVID in the specimens. Also, the behavior of BVID evolution during indentation loading was investigated by the analyzing of AE signals for different damage mechanisms by b-value and sentry function methods. Then, similar specimens were subjected to LVI loading with various impact energy levels and the induced BVID was studied using the behavior of the load curves and C-scan and digital camera images. Although the general behavior of the specimens under quasi-static indentation and LVI tests has a considerable similarity, there are two differences that should be considered if quasi-static indentation test is taken instead of LVI test to better study of BVID; the higher critical load (42.6% and 58.2% for S_D and S_B , respectively) and lower area of the delaminated region (2% and 10% for S_D and S_B , respectively) in LVI test in comparison to quasi-static indentation test. In order to specify the percentage of each damage mechanism in BVID of the impacted specimens, the AE signals of the impacted specimens were analyzed by WPT and energy criterion methods. The percentage of interlaminar and intralaminar damages in the LVI test specimens had a good consistency with the quasi-static indentation test results. This shows that AE is a powerful and reliable technique for assessment of BVID and also structural health monitoring of laminated composite structures.

References

- [1] Tan W, Falzon BG, Chiu LNS, Price M. Predicting low velocity impact damage and Compression-After-Impact (CAI) behaviour of composite laminates. *Composites Part A* 2015; 71: 212–26.
- [2] Shi Y, Swait T, Soutis C. Modelling damage evolution in composite laminates subjected to low velocity impact. *Compos Struct* 2012; 94: 2902–13.
- [3] Wagih A, Maimí P, Blanco N, Costa J. A quasi-static indentation test to elucidate the sequence of damage events in low velocity impacts on composite laminates. *Composites Part A* 2016; 82: 180–9.
- [4] Hu N, Zemba Y, Okabe T, Yan C, Fukunaga H, Elmarakbi AM. A new cohesive model for simulating delamination propagation in composite laminates under transverse loads. *Mech Mater* 2008; 40: 920–35.
- [5] Andrew JJ, Arumugam V, Santulli C. Effect of post-cure temperature and different reinforcements in adhesive bonded repair for damaged glass/epoxy composites under multiple quasi-static indentation loading. *Compos Struct* 2016; 143: 63–74.
- [6] Sun XC, Hallett SR. Barely visible impact damage in scaled composite laminates: Experiments and numerical simulations. *Int J Impact Eng* 2017; 109: 178-95.
- [7] He Y, Tian GY, Pan M, Chen D. Non-destructive testing of low-energy impact in CFRP laminates and interior defects in honeycomb sandwich using scanning pulsed eddy current. *Composites Part B* 2014; 59: 196-203.
- [8] Dionysopoulos D, Fierro GPM, Meo M, Ciampa F. Imaging of barely visible impact damage on a composite panel using nonlinear wave modulation thermography. *NDT and E Int* 2018; 95: 9-16.
- [9] Sikdar S, Kudela P, Radziński M, Kundu A, Ostachowicz W. Online detection of barely visible low-speed impact damage in 3D-core sandwich composite structure. *Compos Struct* 2018; 185: 646-55.
- [10] Toivola R, Lai PN, Yang J, Jang SH, Jen AKY, Flinn BD. Mechanochromic fluorescence in epoxy as a detection method for barely visible impact damage in CFRP composites. *Compos Sci Technol* 2017; 139: 74-82.

- [11] Kudela P, Radzienski M, Ostachowicz W. Impact induced damage assessment by means of Lamb wave image processing. *Mech Syst Sig Process* 2018; 102: 23-36.
- [12] Polimeno U, Meo M. Detecting barely visible impact damage detection on aircraft composites structures. *Compos Struct* 2009; 91(4): 398-402.
- [12] Klepka A, Pieczonka L, Staszewski WJ, Aymerich F. Impact damage detection in laminated composites by non-linear vibro-acoustic wave modulations. *Composites Part B* 2014; 65: 99-108
- [14] Dziendzikowski M, Kurnyta A, Dragan K, Klysz S, Leski A. In situ Barely Visible Impact Damage detection and localization for composite structures using surface mounted and embedded PZT transducers: A comparative study. *Mech Syst Sig Process* 2016; 78: 91-106.
- [15] Katunin A, Dragan K, Dziendzikowski M. Damage identification in aircraft composite structures: A case study using various non-destructive testing techniques. *Compos Struct* 2015; 127: 1-9.
- [16] Mustapha S, Ye L, Dong X, Alamdari MM. Evaluation of barely visible indentation damage (BVID) in CF/EP sandwich composites using guided wave signals. *Mech Syst Sig Process Processing* 2016; 76–77: 497–517.
- [17] Saeedifar M, Fotouhi, Ahmadi Najafabadi M, Hosseini Toudeshky H, Minak G. Prediction of quasi-static delamination onset and growth in laminated composites by acoustic emission. *Composites Part B* 2016; 85:113-22
- [18] Loutas T, Eleftheroglou N, Zarouchas D. A data-driven probabilistic framework towards the in-situ prognostics of fatigue life of composites based on acoustic emission data. *Compos Struct* 2017; 161: 522-9.
- [19] Haggui M, Mahi AE, Jendli Z, Akrouf A, Haddar M. Static and fatigue characterization of flax fiber reinforced thermoplastic composites by acoustic emission. *Appl Acoust* 2018; <https://doi.org/10.1016/j.apacoust.2018.03.011>.
- [20] Maleki A, Saeedifar M, Ahmadi Najafabadi M, Zarouchas D. The fatigue failure study of repaired aluminum plates by composite patches using Acoustic Emission. *Eng Fract Mech* 2017; <https://doi.org/10.1016/j.engfracmech.2017.12.034>.

- [21] Eleftheroglou N, Zarouchas D, Loutas T, Alderliesten R, Benedictus R. Structural health monitoring data fusion for in-situ life prognosis of composite structures. *Reliab Eng Syst Saf* 2018; 178: 40-54.
- [22] Zarif Karimi N, Minak G, Kianfar P, Analysis of damage mechanisms in drilling of composite materials by acoustic emission. *Compos Struct* 2015; 131: 107-14.
- [23] Pashmforoush F, Khamedi R, Fotouhi M, Hajikhani M, Ahmadi M. Damage classification of sandwich composites using acoustic emission technique and k-means genetic algorithm. *J Nondestr Eval* 2014; 33(4): 481–92.
- [24] Mohammadi R, Ahmadi Najafabadi M, Saeedifar M, Yousefi J, Minak G. Correlation of acoustic emission with finite element predicted damages in open-hole tensile laminated composites. *Composites Part B* 2017; 108: 427-35.
- [25] Abir MR, Tay TE, Ridha M, Lee HP. Modelling damage growth in composites subjected to impact and compression after impact. *Compos Struct* 2017; 168: 13–25.
- [26] Singh H, Namala KK, Mahajan P. A damage evolution study of E-glass/epoxy composite under low velocity impact. *Composites Part B* 2015; 76: 235–48.
- [27] Jung KH, Kim DH, Kim HJ, Park SH, Jhang KY, Kim HS. Finite element analysis of a low-velocity impact test for glass fiber-reinforced polypropylene composites considering mixed-mode interlaminar fracture toughness. *Compos Struct* 2017; 160: 446–56.
- [28] Aymerich F, Dore F, Priolo P. Simulation of multiple delaminations in impacted cross-ply laminates using a finite element model based on cohesive interface elements. *Compos Sci Technol* 2009; 69: 1699–709.
- [29] Singh H, Mahajan P. Analytical modeling of low velocity large mass impact on composite plate including damage evolution. *Compos Struct* 2016; 149: 79–92.
- [30] Panettieri E, Fanteria D, Montemurro M, Froustey C. Low-velocity impact tests on carbon/epoxy composite laminates: a benchmark study. *Composites Part B* 2016; 107: 9–21.
- [31] Boominathan R, Arumugam V, Santulli C, Adhithya Plato Sidharth A, Anand Sankar R, Sridhar BTN. Acoustic emission characterization of the temperature effect on falling weight impact damage in carbon/epoxy laminates. *Composites Part B* 2014; 56: 591-8.

- [32] Saeedifar M, Ahmadi Najafabadi M, Zarouchas D, Hosseini Toudeshky H, Jalalvand M. Clustering of interlaminar and intralaminar damages in laminated composites under indentation loading using acoustic emission. *Composites Part B* 2018; 144: 206-19.
- [33] Suresh Kumar C, Arumugam V, Santulli C. Characterization of indentation damage resistance of hybrid composite laminates using acoustic emission monitoring. *Composites Part B* 2017; 111: 165-78.
- [34] Hexcel Product Data. HexPly® 8552 Epoxy matrix (180°C/356°F curing matrix). Hexcel Composites Publication; 2013. FTA 072e.
- [35] Hexcel Marlett K. 8552 IM7 unidirectional prepregs 190 gsm & 35%RC qualification material property data report CAM-RP-2009-015 National Institute for Aviation Research; 2011.
- [36] ASTM D7136/D7136M-12. Measuring the Damage Resistance of a Fiber-Reinforced Polymer Matrix Composite to a Drop-Weight Impact Event. ASTM International, West Conshohocken, PA, 2012.
- [37] ASTM E976-10. Standard guide for determining the reproducibility of acoustic emission sensor response. ASTM International, West Conshohocken, PA, 2010.
- [38] Gutenberg B, Richter CF. In seismicity of the Earth and associated phenomenon. 2nd ed., Princeton University Press, Princeton, NJ, USA, 1954.
- [39] Sagasta F, Zitto ME, Piotrkowski R, Benavent-Climent A, Suarez E, Gallego A. Acoustic emission energy b-value for local damage evaluation in reinforced concrete structures subjected to seismic loadings. *Mech Syst Sig Process* 2018; 102: 262-77.
- [40] Ma G, Li H. Acoustic emission monitoring and damage assessment of FRP-strengthened reinforced concrete columns under cyclic loading. *Constr Build Mater* 2017; 144: 86-98.
- [41] Carnì DL, Scuro C, Lamonaca F, Olivito RS, Grimaldi D. Damage analysis of concrete structures by means of acoustic emissions technique. *Composites Part B* 2017; 115: 79-86.
- [42] Minak G, Zucchelli A. Damage evaluation and residual strength prediction of CFRP laminates by means of acoustic emission techniques. In: Durand LP, editor. *Composite Materials Research Progress*, New York: Nova Science Publishers Inc. 2008; 165– 207.

- [43] Wickerhauser, MV. Adapted wavelet analysis from theory to software. IEEE Press, 1994.
- [44] Fotouhi M, Heidary H, Ahmadi M, Pashmforoush F. Characterization of composite materials damage under quasi-static three-point bending test using wavelet and fuzzy C-means clustering. J Compos Mater 2012; 46 (15): 1795-808.
- [45] Soman KP, Ramachandran KI, Resmi NG. Insight Into Wavelets: from Theory to Practice. 3rd edition, PHI Learning Pvt. Ltd., 2010.
- [46] Heracovich CT. Mechanics of fibrous composites. John Wiley & Sons, USA, 1998; 255-8.
- [47] Suemasu H, Majima O. Multiple delaminations and their severity in circular axisymmetric plates subjected to transverse loading. J Compos Mater 1996; 30: 441–53.

List of Figure captions

Fig. 1. a) Quasi-static indentation, and b) low-velocity impact test setups.

Fig. 2. A schematic of the WPT tree (L: low frequency part (approximation), and H: high frequency part (detail)).

Fig. 3. The load-displacement curve of the specimens and the ultrasonic C-scan images at different stages of loading.

Fig. 4. A cross-section overview of midplane of the longitudinal direction for a) S_D -after the elastic region, b) S_D -final fracture, c) S_B - after the elastic region, d) S_B -final fracture [32].

Fig. 5. The clustered AE data of different damage mechanisms in the quasi-static indentation tests [32].

Fig. 6. The b-value and sentry function curves of matrix cracking for specimen a) S_D and b) S_B .

Fig. 7. The b-value and sentry function curves of delamination for specimen a) S_D and b) S_B .

Fig. 8. The b-value and sentry function curves of fiber breakage for specimen a) S_D and b) S_B .

Fig. 9. The load-time curve and the ultrasonic C-scan images of impact tests for specimen a) S_D , and b) S_B .

Fig. 10. A cross-section overview of midplane of the longitudinal direction for the impacted specimens.

Fig. 11. The load- deflection curves of LVI and indentation tests for specimen a) S_D , and b) S_B .

Fig. 12. a) An AE waveform recorded during the impact test, and b) the frequency distribution of the AE signal obtained by FFT.

Fig. 13. a) The energy content, and b) the frequency content for each WPT component of the decomposed AE signals of specimen S_B under impact 20 J.

List of Table captions

Table 1. The physical and mechanical properties of IM7/8552 [34, 35].

Table 2. Configurations of the specimens.

Table 3. The corresponded load to the initial delamination growth in indentation and LVI tests.

Table 4. Area of the delaminated region for the indentation and impact tests' specimens.

Table 5. The energy percentage of interlaminar and intralaminar damage mechanisms in the LVI specimens obtained from WPT and energy criterion.